Spinel ferrite nanocrystals embedded inside ZnO: Magnetic, electronic, and magnetotransport properties

Shengqiang Zhou (周生强),[1,*] K. Potzger,[1] Qingyu Xu (徐庆宇),[2] K. Kuepper,[1] G. Talut,[1] D. Markó,[1] A. Mücklich,[1] M. Helm,[1] J. Fassbender,[1] E. Arenholz,[3] and H. Schmidt[1]

[1]*Institute of Ion Beam Physics and Materials Research, Forschungszentrum Dresden-Rossendorf, P.O. Box 510119, 01314 Dresden, Germany*

[2]*Department of Physics, Southeast University, Nanjing 211189, China*

[3]*Advanced Light Source, Lawrence Berkeley National Laboratory, Berkeley, California 94720, USA*

(Received 7 November 2008; revised manuscript received 21 August 2009; published 18 September 2009)

In this paper we show that spinel ferrite nanocrystals ($NiFe_2O_4$, and $CoFe_2O_4$) can be texturally embedded inside a ZnO matrix by ion implantation and postannealing. The two kinds of ferrites show different magnetic properties, e.g., coercivity and magnetization. Anomalous Hall effect and positive magnetoresistance have been observed. Our study suggests a ferrimagnet/semiconductor hybrid system for potential applications in magnetoelectronics. This hybrid system can be tuned by selecting different transition-metal ions (from Mn to Zn) to obtain various magnetic and electronic properties.

DOI: 10.1103/PhysRevB.80.094409 PACS number(s): 75.75.+a, 75.50.Pp, 78.70.Dm, 72.25.Dc

I. INTRODUCTION

Spinel ferrites are materials with rich magnetic and electronic properties.[1] As bulk materials, they can be half metallic (such as Fe_3O_4) or insulating (most spinel ferrites), ferrimagnetic (most spinel ferrites) or antiferromagnetic ($ZnFe_2O_4$). Insulating ferrites (such as $NiFe_2O_4$ and $ZnNiFe_2O_4$) are usually referred to as magnetic insulators. These kinds of materials are technologically important with various applications as permanent magnets, microwave devices, and magnetic recording media. Physically the magnetic and electronic properties of spinel ferrites are determined by the cation distribution among the tetrahedral (*A*) and octahedral (*B*) sites. The growth of low-dimensional spinel ferrites of both thin films and nanoparticles has shown the possibility to tune the cation distribution, therefore resulting in magnetic and electrical properties drastically different from bulk materials. Lüders *et al.*[2] have shown that the conductivity of $NiFe_2O_4$ thin films can be tuned over 5 orders of magnitude by varying the growth atmosphere. The sites of Fe^{3+} can be changed from *A* to *B* sites in $ZnFe_2O_4$ nanoparticles, resulting in ferrimagnetism.[3] Geiler *et al.*[4] proposed a method to design and control the cation distribution in hexagonal $BaFe_{12-x}Mn_xO_{19}$ ferrites at an atomic scale, which results in the increase in magnetic moment and Néel temperature. Moreover, most of transition metals can form solid solutions with Fe_3O_4, resulting in $TM_xFe_{3-x}O_4$ spinel alloys with x ranging from 0 to 1, which provides an additional degree of freedom to tune their magnetic and electronic properties.[5,6] In previous research, anomalous Hall effect and magnetoresistance have been found in spinel ferrite thin films or granules at room temperature, demonstrating spin polarization of free carriers. Moreover, ferrite thin films $NiFe_2O_4$ and $CoFe_2O_4$ with different conductivities have been demonstrated to be useful as electrodes or spin filter in magnetic tunnel junctions.[2,7–10] However, to our knowledge, very limited effort has been spent to integrate ferrite oxides with semiconductors. The growth of ferrite oxides requires high temperatures and oxygen environment, which is detrimental to conventional semiconductors such as Si and GaAs.[11] This explains why oxide insulators such as MgO, Al_2O_3, and $SrTiO_3$ are mostly used as the substrates to grow ferrite oxides.[12] In this paper, we show that $TMFe_2O_4$ nanocrystals (TM=Ni,Co) can be embedded inside ZnO and we present a systematic study on their magnetic, electronic, and transport properties. The various ferrites with different magnetic properties synthesized inside a semiconducting matrix open an avenue for fabricating hybrid systems.

II. EXPERIMENTS

We utilize different methods to characterize the ferrite/ZnO hybrid systems. The aim is to show the similarity in structure but variability in magnetic, electronic, and magnetotransport properties.

Commercial ZnO(0001) single crystals with the thickness of 0.5 mm from Crystec were coimplanted with ^{57}Fe and Ni or Co ions at 623 K with a fluence of 4×10^{16} and 2×10^{16} cm^{-2}, respectively. The implantation energy was 80 keV for all three kinds of elements. This energy resulted in the projected range of R_P=38,37,37 nm and the longitudinal straggling of ΔR_P=17,17,17 nm, respectively, for Fe, Co, and Ni. Therefore, the implanted Fe ions are in the same range as the Co and Ni ions. The maximum atomic concentration is about 10% and 5% for Fe and Ni(Co), respectively (TRIM code[13]). The maximum implanted depth is around 80 nm (around 5% of the maximum concentration) from the surface. Annealing was performed in a high-vacuum (base pressure $\leq10^{-6}$ mbar) furnace at 1073 K for 60 min. In our previous study we have performed detailed annealing investigation for transition-metal-implanted ZnO single crystals.[3,14,15] Briefly, more metallic clusters formed when annealing at mild temperatures (823 or 923 K) while the oxidation starts at around 1073 K. Keeping this high temperature, a longer annealing time results in the formation of ferrites in Fe-implanted ZnO.

Magnetic properties were measured with superconducting quantum interference device (SQUID, Quantum Design

MPMS) magnetometery. The samples were measured with the field along the sample surface. The temperature-dependent magnetization measurement was carried out in the following way. The sample was cooled in zero field from above room temperature to 5 K. Then a 50 Oe field was applied and the zero-field-cooled (ZFC) magnetization curve was measured with increasing temperature from 5 to 350 K, after which the field-cooled (FC) magnetization curve was measured in the same field from 350 to 5 K with decreasing temperature.

Structural analysis was performed by synchrotron-radiation x-ray diffraction (SR-XRD) and transmission electron microscopy (TEM, FEI Titan). SR-XRD was performed at the Rossendorf beamline (BM20) at the ESRF with an x-ray wavelength of 0.154 nm. The cross-section specimen for TEM investigation was prepared by the conventional method including cutting, glueing, mechanical polishing, and dimpling procedures followed by Ar^+ ion-beam milling until perforation. The ion milling was performed using a "Gatan PIPS." The milling parameters were 4 keV, 10 μA ion current at milling angle of 4° with respect to the specimen surface. The area around the hole is electron transparent (thickness <100 nm).

Element-specific electronic properties were investigated by x-ray absorption spectroscopy (XAS) and x-ray magnetic circular dichroism (XMCD) at the Fe, Co, and Ni $L_{2,3}$ absorption edges. These experiments were performed at beamlines 8.0.1 (XAS) and 6.3.1 (XMCD) of the advanced light source in Berkeley, respectively. Both total electron yield (TEY) and total fluorescence yield (TFY) were recorded during the measurement. While TFY is bulk sensitive, TEY probes the near-surface region. For XMCD, the measurement was done at the minimum achievable measurement temperature of 23 K in TEY mode. A magnetic field of ± 2000 Oe was applied parallel to the beam. The grazing angle of the incident light was fixed at 30° with respect to the sample surface.

Conversion electron Mössbauer spectroscopy (CEMS) in constant-acceleration mode at room temperature (RT) was used to investigate the Fe lattice sites, electronic configuration, and corresponding magnetic hyperfine fields. The spectra were evaluated with Lorentzian lines using a least-squares fit.[16] All isomer shifts are given with respect to α-Fe at RT.

Magnetotransport properties were measured using Van der Pauw geometry with a magnetic field applied perpendicular to the film plane. Fields up to 60 kOe were applied over a wide temperature range from 5 to 290 K and the carrier-concentration and the majority-carrier mobility were extracted.

III. RESULTS AND DISCUSSION

A. Structural properties

1. X-ray diffraction

Figure 1 shows the SR-XRD patterns for the annealed samples. Besides the strong peaks from ZnO(0002) and (0004), four small peaks arise for each sample. They are assigned to (111), (222), (333), and (444) diffractions for

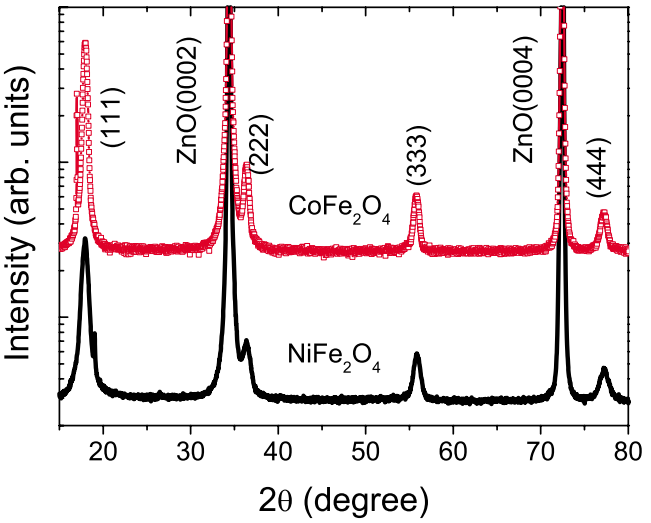

FIG. 1. (Color online) SR-XRD 2θ-θ scan revealing the formation of $NiFe_2O_4$ and $CoFe_2O_4$ in (Ni, Fe) or (Co, Fe) coimplanted ZnO. In both pattern, the diffraction peaks of (111), (222), (333), and (444) from ferrites are clearly visible. The diffraction peaks (0002) and (0004) from ZnO are also indicated. The small and sharp peaks at the left side of $CoFe_2O_4$(111) and the right side of $NiFe_2O_4$(111) cannot be identified at this stage. The peak at the left side of $CoFe_2O_4$(111) could be the forbidden peak of ZnO(0001), which appears due to the lattice damage. However, another forbidden peak of ZnO(0003) does not show up. Note that the two peaks in the two spectra are not at the same angular position and both correspond to very large lattice distances. Some noiselike peaks are also shown in other paper (Ref. 17) and could not be identified.

$NiFe_2O_4$ and $CoFe_2O_4$, respectively. This implies that these nanocrystals are (111) textured inside the ZnO matrix. However, some nanocrystals with (400) orientation have been also observed by TEM as shown below. The crystallite size is estimated using the Scherrer formula.[18]

$$d = 0.9\lambda/(\beta \cdot \cos\,\theta), \tag{1}$$

where λ is the wavelength of the x ray, θ is the Bragg angle, and β is the FWHM of 2θ in radians. The average crystallite size is deduced to be around 12 and 15 nm for $NiFe_2O_4$ and $CoFe_2O_4$ nanocrystals, respectively.

2. TEM

In order to confirm the formation of ferrite nanocrystals, high-resolution cross-section TEM was performed on selected samples. Figure 2(a) displays the bright-field TEM images. In an overview, there are three features. The grains of secondary phases are located in the surface region, which are identified as $NiFe_2O_4$. Some planar extended defects are indicated by arrows and are parallel to the basal plane of the ZnO wurtzite structure in a depth of around 60 nm. These extended defects are caused by ion implantation in ZnO (Ref. 19) and are usually populated at the end of the ion range. The third feature is the dark spot, which is also located in the depth of unimplanted ZnO. The formation of $NiFe_2O_4$ at the near-surface depth is also confirmed by the dark-field TEM image as shown in Fig. 2(b) of the same area

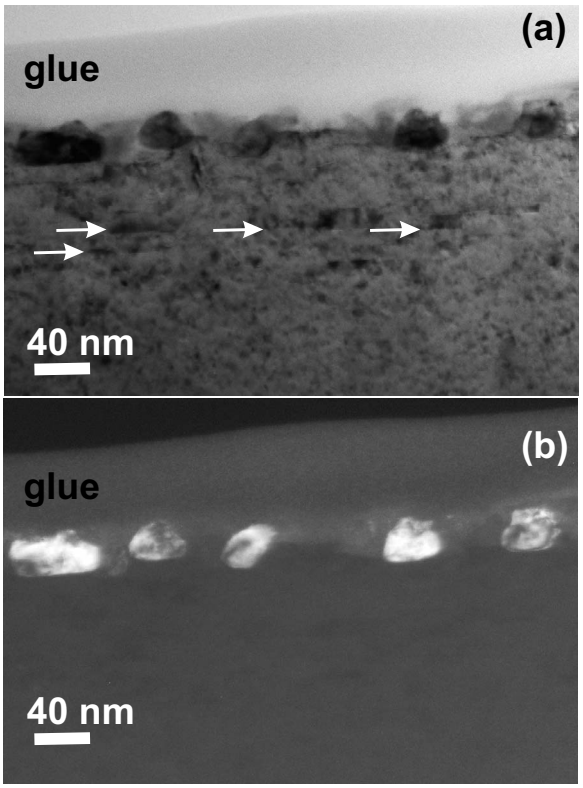

FIG. 2. Cross-section TEM image of Fe and Ni coimplanted ZnO after annealing (a) bright field and (b) dark field.

of Fig. 2(a). The outdiffusion of Fe upon annealing at high temperatures has been observed in ZnO (Ref. 20) as well as in TiO_2.[21]

Using high-resolution TEM we identified the secondary phase to confirm the XRD results. As shown in Fig. 3(a), the sample was tilted in order to have a better view on the nanocrystals. Note that the lattice planes are more clear in the nanocrystals than that in the ZnO substrate. The inset of Fig. 3(a) is the fast Fourier transform (FFT) of the image indicated by a square. The FFT clearly shows the cubic symmetry of the nanocrystal. The two sets of lattice spacings amount to 0.291 and 0.207 nm, and correspond to $NiFe_2O_4$(220) and (004), respectively. Concerning the orientation between $NiFe_2O_4$ and the ZnO matrix, XRD, in general, provides the integral information over a large area of the sample while TEM is a rather localized method. By high-resolution TEM, we found some grains with [111] orientation as shown in Fig. 3(b). By FFT two sets of lattice planes are identified to $NiFe_2O_4${111}. One is parallel with the sample surface while the other is around 71° away from the surface [ZnO(0001)]. This is in agreement with a fcc structure of $NiFe_2O_4$. However there are also some grains with [001] orientation, e.g., the one in Fig. 3(a). One also can see some moiré fringes in the ZnO part due to the overlap of $NiFe_2O_4$ and ZnO.

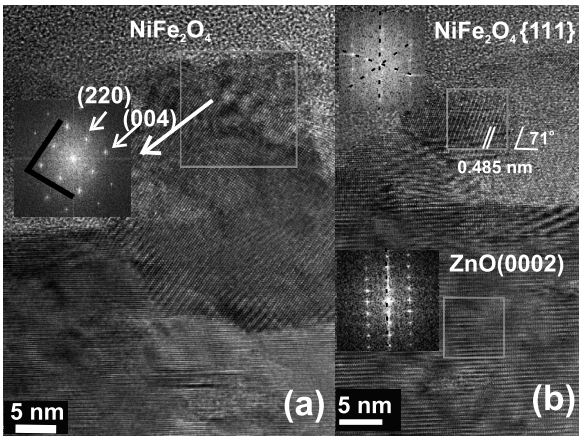

FIG. 3. High-resolution TEM image for representative $NiFe_2O_4$ nanocrystals. (a) The specimens are tilted by 11°. $NiFe_2O_4$ nanocrystal is identified. The black lines guide the eyes to show the cubic symmetry of the secondary phase. (b) Another $NiFe_2O_4$ nanocrystals with the orientation of (111)‖ZnO(0001) as confirmed by FFT patterns. The clearly visible planes are $NiFe_2O_4(\bar{1}11)$ with an angle of ~71° from the surface. In FFT patterns the dashed lines indicate the sets of lattice planes.

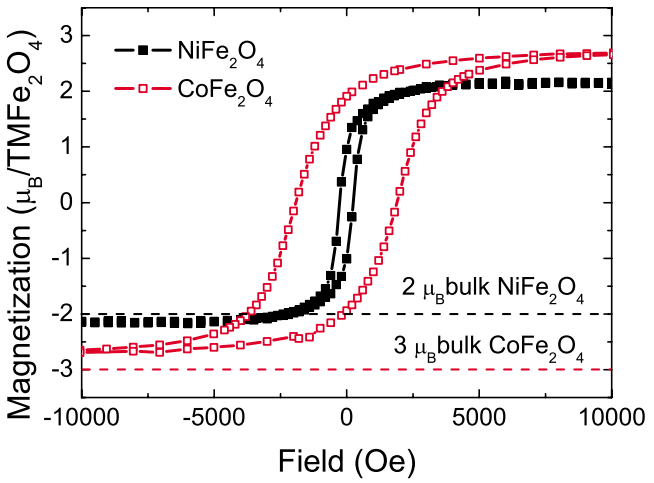

FIG. 4. (Color online) Hysteresis loops measured at 5 K for $NiFe_2O_4$ and $CoFe_2O_4$ nanocrystals. They show drastic difference in coercivity field.

Note that the $NiFe_2O_4$ grains (see Fig. 2) are as large as 20–40 nm and larger than the values determined from XRD. However, one grain does not have to correspond to one $NiFe_2O_4$ nanocrystal. On the other hand, in the dark-field image all the grains show similar sizes as that in the bright field. This is due to the fact that these nanocrystals are well oriented. By high-resolution TEM we examined more than ten nanocrystals in different areas of the specimens. Their diameters are in the range of 10–20 nm, which is in a qualitative agreement with the XRD measurement.

B. Magnetic properties

By structural analysis, we have shown the formation of $NiFe_2O_4$ and $CoFe_2O_4$ nanocrystals inside the ZnO matrix. In this section, we will compare their magnetic properties. Figure 4 shows the hysteresis loops measured at 5 K. The differences between $NiFe_2O_4$ and $CoFe_2O_4$ are significant. At 5 K, the coercivity of $CoFe_2O_4$ is 1900 Oe and much larger than the coercivity of $NiFe_2O_4$ amounting to 280 Oe,

i.e., one is a hard magnet and the other is a soft one. For comparison the saturation magnetization of bulk crystals is also indicated in Fig. 4. $NiFe_2O_4$ nanocrystals have a slightly larger value than bulk $NiFe_2O_4$, and a smaller value for $CoFe_2O_4$ nanocrystals. This could be due to the cation-site exchange between Ni^{2+}, (Co^{2+}), and Fe^{3+} and will be discussed in Sec. III C. However, another possibility is that there is a mixture of Ni^{2+} and Fe^{2+} at tetrahedral sites resulting in $(Ni,Fe)Fe_2O_4$ ($Ni_{1-x}Fe_{2+x}O_4$). The magnetization for bulk Fe_3O_4 is 4.1 μ_B per formula unit. To verify this, one needs to perform a precise local Fe, Ni(Co) concentration measurement. We performed an electron energy-loss spectroscopy (EELS) analysis to profile the composition of the ferrite nanocrystals during the TEM measurements. We could not probe an elementally resolvable EELS signal possibly due to the similar atomic number of the embedding ZnO matrix and the ferrite, given the complex element types (Fe, Co/Ni, and Zn) within the probe area. Macroscopically, the appearance of Fe, Co, and Ni is clearly revealed by x-ray absorption as shown later in Sec. III C. In literature the application of EELS in similar cases (embedded nanocrystals) is mainly for qualitative investigation.[22–24] On the other hand, exposing the nanocrystals to the electron beam for a longer time results in a heavy beam damage and contamination of the specimens, as well as the structural modification of the nanocrystals.[25,26]

Figure 5 shows the temperature-dependent saturation magnetization and coercivity. One sees clearly that the coercivity decreases exponentially with increasing temperature. This is expected for a magnetic nanoparticle system. According to the Stoner-Wohlfarth theory,[26] the magnetic anisotropy energy E_A of a single domain particle can be expressed as

$$E_A = KV \sin^2 \theta, \tag{2}$$

where K is the magnetocrystalline anisotropy constant, V is the volume of the nanoparticle, and θ is the angle between the magnetization direction and the easy axis of the nanoparticle. This anisotropy serves as the energy barrier to prevent the change in magnetization direction. When the size of magnetic nanoparticles is reduced to a critical value, E_A is comparable with thermal activation energy, k_BT, the magnetization direction of the nanoparticle can be easily moved away from the easy axis by thermal activation and/or an external magnetic field. The coercivity of the nanoparticles is closely related to the magnetic anisotropy. At a temperature below blocking temperature T_B, the coercivity corresponds to a magnetic field which provides the required energy in addition to the thermal activation energy to overcome the magnetic anisotropy. As temperature increases, the required magnetic field (H_C) for overcoming the anisotropy decreases. At the temperature of 0 K, where all the magnetic moments are blocked, the coercivity is equal to the value for single domains. At a high enough temperature, when all moments fluctuate with a relaxation time shorter than the measuring time, coercivity equals zero. In the temperatures between the two extremes the coercivity H_C can be evaluated by the following formula:[27]

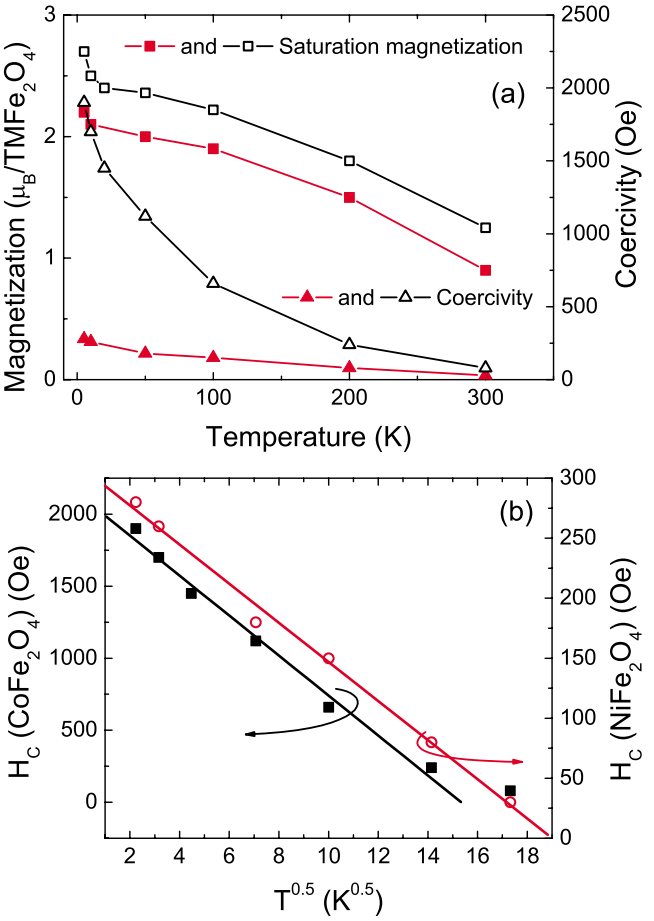

FIG. 5. (Color online) (a) Temperature-dependent saturation magnetization and coercivity for $NiFe_2O_4$ (red solid symbols) and $CoFe_2O_4$ (black open symbols). The solid lines are guides for eyes. (b) The plot of coercivity as a function of $T^{1/2}$.

$$H_C = H_{C0}\left[1 - \left(\frac{T}{T_B}\right)^{1/2}\right], \tag{3}$$

where H_{C0} is the coercivity at 0 K and T_B is the blocking temperature. Figure 5(b) shows a plot of H_C as a function of $T^{1/2}$. For the $NiFe_2O_4$ system H_C roughly obeys a linear dependence on $T^{1/2}$ in the whole measured temperature range. The deduced blocking temperature lies around 360 K, which is rather close to the value found by the ZFC/FC magnetization as shown below. The poor fitting for the $CoFe_2O_4$ system may be due to the fact that the magnetocrystalline anisotropy energy of $CoFe_2O_4$ is much larger (2 orders of magnitude) than $NiFe_2O_4$. For a similar grain size the blocking temperature of $CoFe_2O_4$ can be much higher for $NiFe_2O_4$. In such a case, the measured temperature range is not large enough compared to the high blocking temperature. This results in a large error in the fitting.

Figure 6 shows the ZFC/FC magnetization curves measured at 50 Oe. An irreversible behavior is observed in ZFC/FC curves. Such an irreversibility originates from the anisotropy barrier blocking of the magnetization orientation in the nanoparticles cooled under zero field. The magnetization direction of the nanoparticles is frozen as the initial sta-

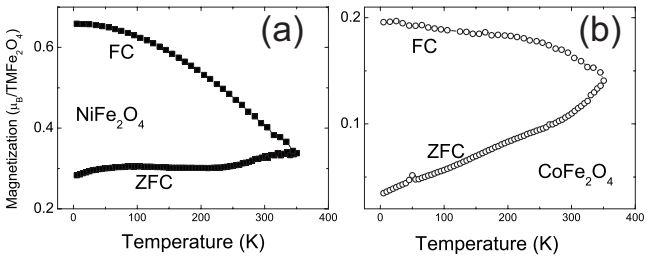

FIG. 6. ZFC/FC magnetization curves measured with a field of 50 Oe. (a) $NiFe_2O_4$ and (b) $CoFe_2O_4$. Up to 350 K, no ZFC maximum was observed for $CoFe_2O_4$.

tus at high temperature, i.e., randomly oriented. At low temperature (5 K in our case), a small magnetic field of 50 Oe is applied. Some small nanoparticles with small magnetic anisotropy energy flip along the field direction while the large ones do not. With increasing temperature, the thermal activation energy together with the field flips the larger particles. This process results in the increase in the magnetization in the ZFC curve with temperature. The size distribution of nanoparticles, i.e., the magnetic anisotropy is usually not uniform in the randomly arranged nanoparticle systems. The larger the particles, the higher the E_A, and a larger k_BT is required to become superparamagnetic. The gradual increase and the small upturn at around 20 K in the ZFC curves is due to the size distribution of nanocrystals. In the ZFC curve for $NiFe_2O_4$ [Fig. 6(a)] a broad maximum is observed at around 330 K while for $CoFe_2O_4$ [Fig. 6(a)] no maximum can be seen up to 350 K. The mean blocking temperature for $CoFe_2O_4$ is well above room temperature, which is evidenced also from the rather large coercivity field of 80 Oe at 300 K (see Fig. 5). Note that the ZFC/FC magnetization of $NiFe_2O_4$ is much smaller than that of $CoFe_2O_4$. This is due to the much larger coercivity field (magnetocrystalline constant K) of $CoFe_2O_4$, which is well above the small applied field of 50 Oe.

Since the blocking temperature is closely related to the magnetic anisotropy energy E_A, one can evaluate the size of nanomagnets by the measured T_B. For a dc magnetization measurement in a small magnetic field by SQUID magnetometry, T_B is given by

$$T_{B,\mathrm{Squid}} \approx \frac{KV}{30k_B}, \tag{4}$$

where K is the anisotropy energy density, V is the particle volume, and k_B is the Boltzmann constant.[28] K is 6.3×10^3 and 4.0×10^5 Jm^{-3} for bulk $NiFe_2O_4$ and $CoFe_2O_4$, respectively, at room temperature.[29,30] Due to its large magnetocrystalline anisotropy the maximum in ZFC curve of $CoFe_2O_4$ nanocrystals cannot be seen within the measured temperature range. That means the blocking temperature is much larger than 350 K, which corresponds to an average diameter of $CoFe_2O_4$ larger than 9 nm if assuming the value of K for a bulk $CoFe_2O_4$. For $NiFe_2O_4$ nanocrystals, K is much smaller. Therefore, we can see a maximum at around 320 K in the ZFC magnetization curve. Using the K value for bulk $NiFe_2O_4$, the average diameter of $NiFe_2O_4$ can be calculated and amounts to 34 nm. This value, however, is larger than that deduced from XRD and TEM measurements. The large discrepancy is resulting from the underestimation of K by assuming the value of a bulk crystal. K can be largely enhanced due to strain and surface effect in $NiFe_2O_4$ nanomagnets but relatively less enhanced in $CoFe_2O_4$.[31] The later has been confirmed in strained epitaxial $CoFe_2O_4$ thin films.[32]

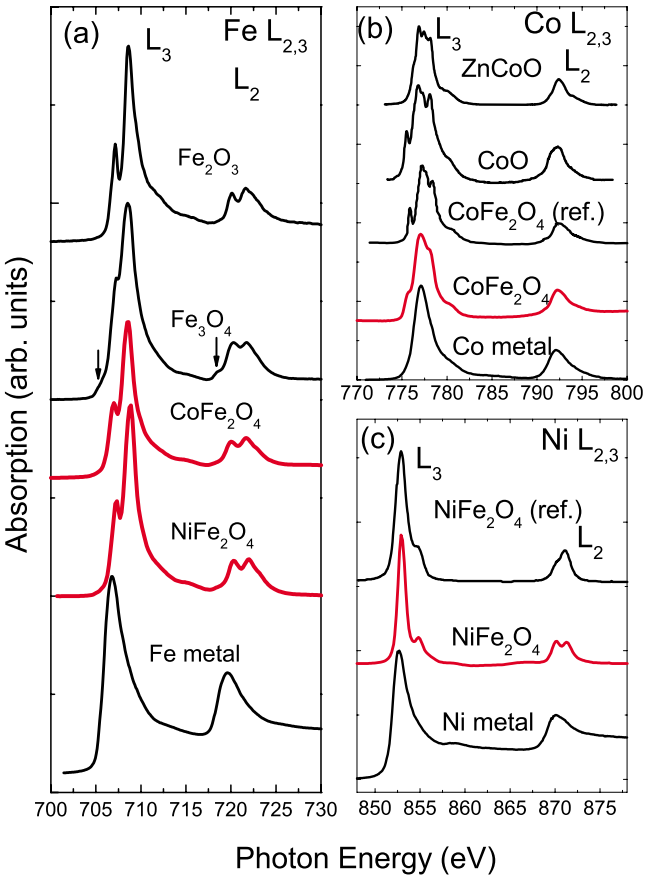

FIG. 7. (Color online) XAS of $NiFe_2O_4$ and $CoFe_2O_4$ along with reference spectra from pure metal and oxides at the (a) Fe $L_{2,3}$ edge, (b) Co $L_{2,3}$ edge and (c) Ni $L_{2,3}$ edge. The reference spectra are taken from published papers: Fe_2O_3 (Ref. 41), Fe_3O_4 (Ref. 41), CoO (Ref. 35), ZnCoO (Ref. 36) $NiFe_2O_4$ (Ref. 40), and $CoFe_2O_4$ (Ref. 37).

C. Electronic configuration

1. X-ray absorption spectra

The magnetic properties of 3*d* transition-metal elements, such as Fe, Co, and Ni are determined by the 3*d* valence electrons, which can be investigated by *L*-edge XAS measurements (transition from the 2*p* shell to the 3*d* shell). Figure 7 shows the $L_{2,3}$ XAS of Fe, Co, and Ni in the two samples, measured in TEY mode. The spectra of pure metals and some oxides are also shown for comparison. The metal spectra mainly show two broad peaks, reflecting the width of the empty *d* bands while the oxide spectra exhibit a considerable fine structure of the *d* bands, the so-called multiplet structure. By comparison with corresponding XAS of pure

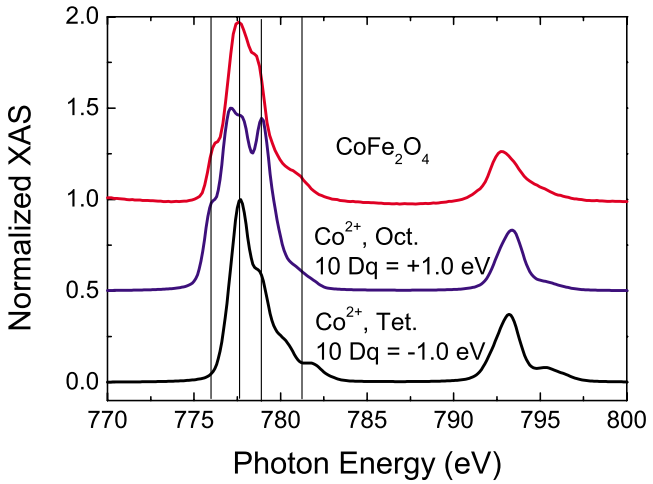

FIG. 8. (Color online) The Co $L_{2,3}$-edge XAS spectrum of $CoFe_2O_4$ along with theoretical calculations for a tetrahedral ($10D_q$=−1 eV) and an octahedral ($10D_q$=+1 eV) coordination of Co ions.

metals, one can qualitatively conclude that metallic Fe, Co, and Ni are not present in the samples. In Fig. 7(a) one can see the multiplet structure of Fe $L_{2,3}$ XAS. The most noticeable feature is the rather pronounced peak at the low-energy part of the L_3 edge. This is a common feature for ferrite materials.[33] Multiplet calculations for FeO and α-Fe_2O_3 reveal that the shoulders at 705.5 and 718.5 eV [indicated by the vertical arrows in the Fig. 7(a)] are associated with Fe^{2+} ions.[34] Note that these features disappear in the spectrum of Fe_2O_3. Following these arguments, the Fe ions in our samples are mainly Fe^{3+} ions.

The Co-L_3 edge [Fig. 7(b)] is composed of a fine structure with four features, a small peak at 775.5 eV, the total maximum in absorption at 777 eV, followed by a shoulder at 778 eV and a further satellite at 780 eV. Since in this sample the Co is in pure Co^{2+} configuration, we can compare the spectrum with reference compounds namely CoO (spectrum taken from Ref. 35) and $Zn_{0.75}Co_{0.25}O$ (spectrum taken from Ref. 36). Co^{2+} ions are at octahedral sites and at tetrahedral sites in CoO and $Zn_{0.75}Co_{0.25}O$, respectively. From the comparison of the overall shape and satellite structure our spectrum is more similar to that of CoO, and also similar to the XAS of $CoFe_2O_4$ presented in Ref. 37. We can conclude that the major part of Co^{2+} ions are at octahedral sites. In order to confirm this conclusion, we performed simulations of the local electronic structure around the Co^{2+} ions by means of full multiplet calculations using the TT-MULTIPLETS program.[38,39] The energy levels of the initial ($2p^63d^7$) and final absorption state ($2p^53d^8$) are calculated by means of the corresponding Slater integrals which are subsequently reduced to 80% (corresponds to their atomic values). Then a tetrahedral or octahedral crystal field was considered using a crystal-field parameter of $10D_q$=−1 eV and $10D_q$=+1 eV, respectively. Finally the calculated spectra were broadened with the experimental resolution for comparison. As displayed in Fig. 8, one can see that the measured spectrum reasonably reproduces the features in the simulated octahedral coordination.

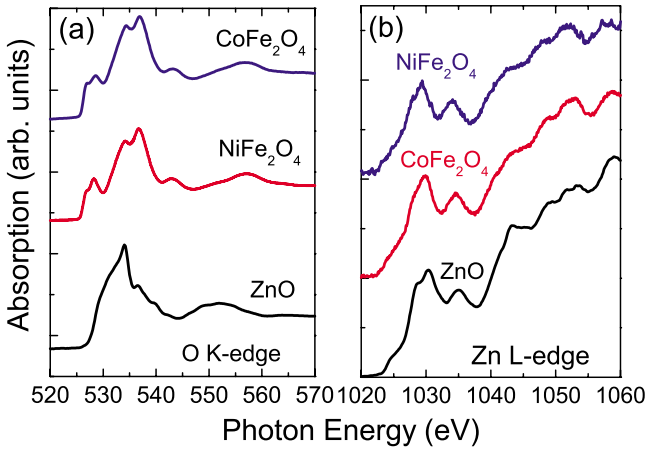

FIG. 9. (Color online) The XA spectra of TEY at the (a) O *K* edge and (b) Zn *L* edge.

Figure 7(c) shows the comparison of Ni $L_{2,3}$ with that in $NiFe_2O_4$.[40] In the paper of Van der Laan *et al.*,[40] the spectrum can be well simulated by considering Ni in an octahedral crystal-field coordination, i.e., Ni ions are fully at octahedral sites. However, the difference between the two spectra is quite clear, especially at the L_2 edge. It could be due to the fact that Ni ions are partially located at tetrahedral sites.

The XAS spectra (Fig. 9) were also recorded at the O *K* edge and Zn *L* edge to prove the formation of ferrites and to check if Zn ions are significantly incorporated into ferrites. All shown spectra were measured in TEY mode, which is more sensitive to the near-surface region where the ferrite nanocrystals were formed. For the O *K* edge, the difference between the $NiFe_2O_4$, $CoFe_2O_4$, and ZnO is very clearly observed, which confirms the coordination change in O ions. Actually the spectra in Fig. 9(a) are very similar to those of Fe_2O_3 and Fe_3O_4.[42] Figure 9(b) shows the comparison of the Zn *L*-edge spectra between ZnO embedded with $NiFe_2O_4$ and $CoFe_2O_4$ nanocrystals, and pure ZnO. The only difference is that the fine structure in the spectrum of ZnO is better resolved. This could be due to the lattice damage in ZnO by ion implantation. No significant amount of Zn has been incorporated into ferrites.

2. XMCD

Correspondingly, XAS recorded at 23 K in TEY (total electron yield) mode at the Fe, Co, and Ni absorption edge revealed a pronounced dichroic behavior under magnetization reversal. XMCD is a difference spectrum of two XA spectra, one taken with left circularly polarized light, and the other with right circularly polarized light.

The XMCD signal at the Fe L_3-edge XMCD for the two samples is shown in Figs. 10(a) and 10(b). From the literature,[43] peak A is attributed to Fe^{2+} at octahedral sites while peaks B and C are due to Fe^{3+} at tetrahedral and octahedral sites, respectively. By comparing the relative height of peak A, B, and C, we can draw some qualitative conclusions on the cation-site distribution in $NiFe_2O_4$ and $CoFe_2O_4$ nanocrystals. Firstly, there are still some Fe^{2+} ions remaining, even if the ratio of implanted Ni (or Co) to Fe is exactly 1:2.

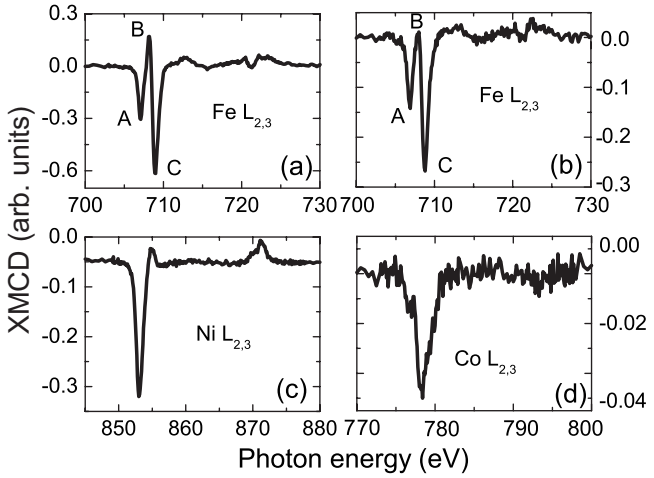

FIG. 10. XMCD at Fe, Ni, and Co $L_{2,3}$ absorption edge. $NiFe_2O_4$: (a) and (c). $CoFe_2O_4$: (b) and (d). Peak labels at Fe L_3 edge: A for Fe^{2+} at octahedral sites, B for Fe^{3+} at tetrahedral sites, and C for Fe^{3+} at octahedral sites (Ref. 43).

This could be due to the fact that Ni(or Co) and Fe ions are not fully chemically reacted at the given annealing condition. Relatively, there are more Fe^{2+} ions at octahedral sites in $CoFe_2O_4$ than in $NiFe_2O_4$. Secondly, part of Fe^{3+} ions are at tetrahedral sites in $NiFe_2O_4$ while in $CoFe_2O_4$ the Fe^{3+} ions are mainly located at octahedral sites. Bulk $NiFe_2O_4$ and $CoFe_2O_4$ are inverse spinels. The Ni^{2+} and Co^{2+} ions are at octahedral sites while half of the Fe^{3+} ions are at octahedral sites and the other half are at tetrahedral sites. With this ordering, the moments of Fe ions at octahedral and tetrahedral sites cancel out, which results in a saturation magnetization of 2 μ_B per $NiFe_2O_4$ formula unit,[44] and 3 μ_B per $CoFe_2O_4$ formula unit.[45] However, in low-dimensional spinels the cation distribution is often different from bulk materials.[44,46] For the case of $NiFe_2O_4$, if all Ni^{2+} replace the Fe^{3+} at tetrahedral sites, resulting in a normal spinel structure, the total magnetic moment can increase up to 4 μ_B per $NiFe_2O_4$ formula. Therefore, the larger magnetic moment in our $NiFe_2O_4$ nanocrystals as shown in Fig. 4 is probably due to a small amount of Ni^{2+} replacing the Fe^{3+} at tetrahedral sites. This cation distribution picture is in agreement with XAS analysis. However, as discussed in Sec. III B, one needs a precise local concentration measurement to verify the ratio Fe:Ni=2:1. Figures 10(c) and 10(d) show the XMCD signal at the $L_{2,3}$ edge for Ni and Co, respectively. They are comparable with corresponding ferrites reported in literature.[33,40] Note the fact that the relative strength of the XMCD signal of $CoFe_2O_4$ is much weaker than that of $NiFe_2O_4$. This is due to their different coercivity fields. Due to the facility capability, a maximum field of 2000 Oe was applied during XAS measurements. The saturation field of $CoFe_2O_4$ is much larger than that of $NiFe_2O_4$ (see Fig. 4).

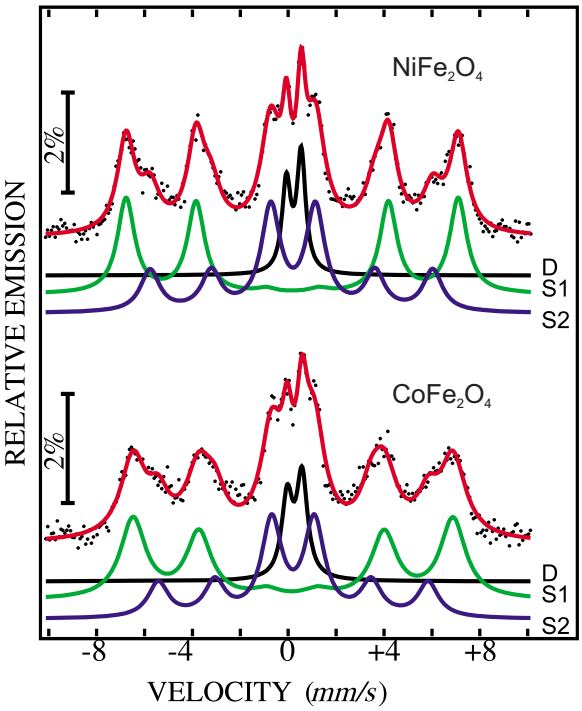

FIG. 11. (Color online) Room-temperature CEMS of $NiFe_2O_4$/ZnO and $CoFe_2O_4$/ZnO composites. The notations for the fitting lines are given as D (doublet) and S1, S2 (sextet).

3. CEMS

CEMS allows one to identify different site occupations, charge, and magnetic states of ^{57}Fe. Figure 11 shows the CEM spectra taken at room temperature for two samples, containing $NiFe_2O_4$ and $CoFe_2O_4$ nanocrystals, respectively. The two samples exhibit similar spectra. Using a least-squares computer program, the spectra can be fitted well by three components. Two sets of sextet hyperfine pattern and one doublet are resolved, all of which are related to Fe^{3+}. The hyperfine parameters calculated according to the evaluations of the spectra are given in Table I. The outer sextet (S1) with a larger magnetic hyperfine field corresponds to octahedral sites while the inner one (S2) with a smaller magnetic hyperfine field to Fe^{3+} at tetrahedral sites.[47–51] This fea-

TABLE I. Hyperfine parameters measured using CEMS for the two samples. The percentage of occupancies of tetrahedral and octahedral sites by Fe^{3+} ions. B_{hf}: hyperfine field, A: relative area of each component, δ: isomer shift and Δ: quadrupole splitting.

	S1 (octahedral)				S2 (tetrahedral)				D		
Sample	B_{hf} (T)	A (%)	δ (mm/s)	Δ (mm/s)	B_{hf} (T)	A (%)	δ (mm/s)	Δ (mm/s)	A (%)	δ (mm/s)	Δ (mm/s)
$NiFe_2O_4$	43	47.7	0.26	0.03	36.5	39	0.28	0.09	13.3	0.34	0.63
$CoFe_2O_4$	41.4	47.1	0.28	0.06	34.9	40.8	0.31	0.05	12.1	0.38	0.62

ture of two sextets is a fingerprint that identifies ferrites. The relative line intensities of the sextets differ from those of a polycrystalline powder material indicating the presence of a texture. Note that the magnetic hyperfine field is considerably smaller than the values of around 50 T for typical $NiFe_2O_4$ or $CoFe_2O_4$,[47,51] which results from the size effect.[50] The doublet (D) is a more questionable component. Most probably it corresponds to smaller ferrite nanocrystals, which are superparamagnetic at room temperature. However, its isomer shift and electric-quadrupole splitting values are considerably larger than the values reported in Ref. 51.

The cation distribution between the two sublattices generally determines the magnetic properties of the spinel system and can be calculated as a ratio between the relative areas of the respective hyperfine field distributions. As shown in Table I, there are more Fe^{3+} ions at octahedral sites for both samples. That means that the $NiFe_2O_4$ and $CoFe_2O_4$ nanocrystals are not purely inverted ferrites and Ni or Co ions partially occupy tetrahedral sites, which is in good agreement with the results of XAS.

D. Magnetotransport properties

Note that both bulk $NiFe_2O_4$ and $CoFe_2O_4$ are insulators with resistivity of 10^2-10^3 Ω cm at room temperature.[2,9] The resistivity of $NiFe_2O_4$ single crystals monotonically increases with decreasing temperature.[52] However, the corresponding thin-film materials can be rather conductive.[2] In Ref. 2, the authors show that the $NiFe_2O_4$ films grown in pure Ar atmosphere have a room-temperature resistivity three orders-of-magnitude smaller (ρ around 100 mΩ cm). The temperature dependence $\rho(T)$ is similar to that of magnetite. On the other hand, ZnO single crystals grown by the hydrothermal method show a high bulk and surface resistivity, with the bulk conduction dominated by a deep donor.[53] Typically, the free charge-carrier concentration amounts to 1×10^{14} cm^{-3} and the mobility to 200 $cm^2\ V^{-1}\ s^{-1}$ (Ref. 54). We measured the temperature dependence of the sheet resistance of the composites of $NiFe_2O_4$ and $CoFe_2O_4$ nanocrystals and ZnO from 20 or 40 to 290 K. Figure 12(a) shows the Arrhenius plot, the sheet resistance R_s on a logarithmic scale as a function of reciprocal temperature. Note that the resistivity of both samples is below 0.1 Ω cm at room temperature assuming a thickness of 80 nm, which is three orders-of-magnitude smaller than that of bulk ferrites or ZnO.[54] The resistance/resistivity of composites of $CoFe_2O_4$ and ZnO is one order smaller than that of $NiFe_2O_4$ and ZnO. The amount of *n*-type defects in ZnO created by means of implantation and annealing is expected to be similar. Therefore, the larger conductivity in the composite of $CoFe_2O_4$ and ZnO is due to the mixing of Fe^{2+} and Fe^{3+} ions at octahedral sites.[2] The temperature dependence of the resistance is more or less the same for both samples. Two different regimes are found. One is the high-temperature part (above 150 K), where the resistance slightly decreases with decreasing temperature. This is a hint of metallic character. However, the electron concentration (around 6×10^{18} cm^{-3} assuming a thickness of 80 nm) as shown in Fig. 12(b) is far below the critical value (4×10^{19} cm^{-3}) of the metal-

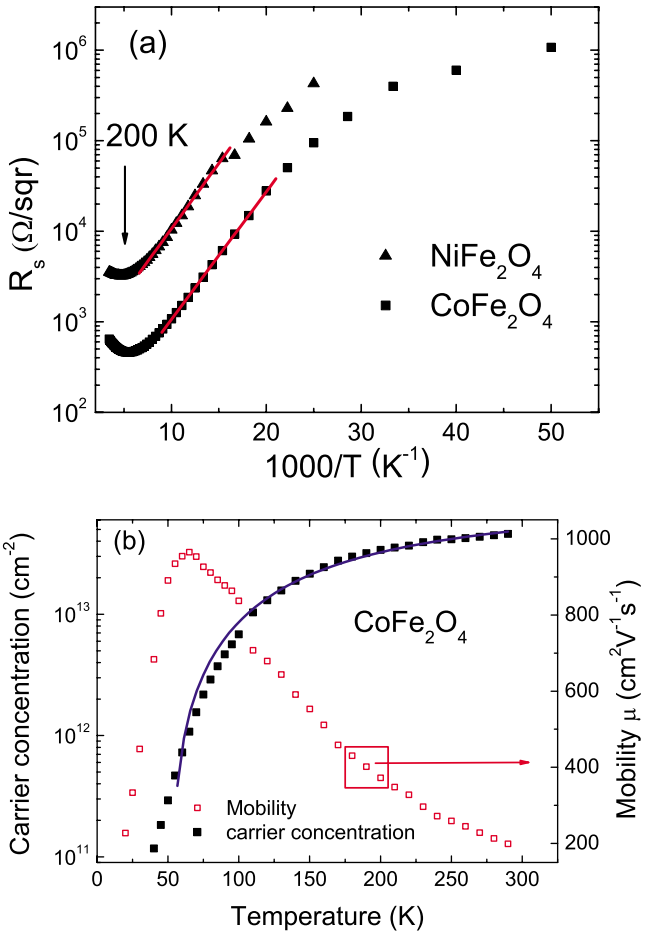

FIG. 12. (Color online) (a) The temperature-dependent sheet resistance (the solid lines show the linear fitting in the temperature range of 60–100 K), and (b) free carrier concentration and mobility of the composites of $NiFe_2O_4$ or $CoFe_2O_4$ nanocrystals and ZnO. The solid line is a fitting of carrier concentration by the function e^{-E_a/k_BT}.

insulator transition in *n*-ZnO.[55] In Refs. 2 and 44, a metallic electrical conductivity has been obtained in ultrathin $NiFe_2O_4$ films, which is attributed to an anomalous distribution of the Fe and Ni cations among tetrahedral and octahedral sites. Therefore, we attribute the metallic character in our samples to the presence of $NiFe_2O_4$ (or $CoFe_2O_4$) nanocrystals. The second regime is in the temperature range below 150 K. In this regime, the samples show a semiconducting conductivity. The thermal activation energy E_a of free carriers can be determined according to the following equation:

$$\rho = e^{E_a/k_BT} + R_{s0}, \tag{5}$$

where k_B is the Boltzmann constant and R_{s0} is a temperature-independent contribution to the resistivity. In Fig. 12(a) the solid lines show the fitting, resulting in a thermal activation energy of ~28 meV for both samples. A similar thermal activation energy of 21 meV has been found in hydrothermally grown ZnO single crystals after high-temperature annealing.[53] At low temperatures the impurities freeze out. In Ref. 52, the authors show that in their measured temperature

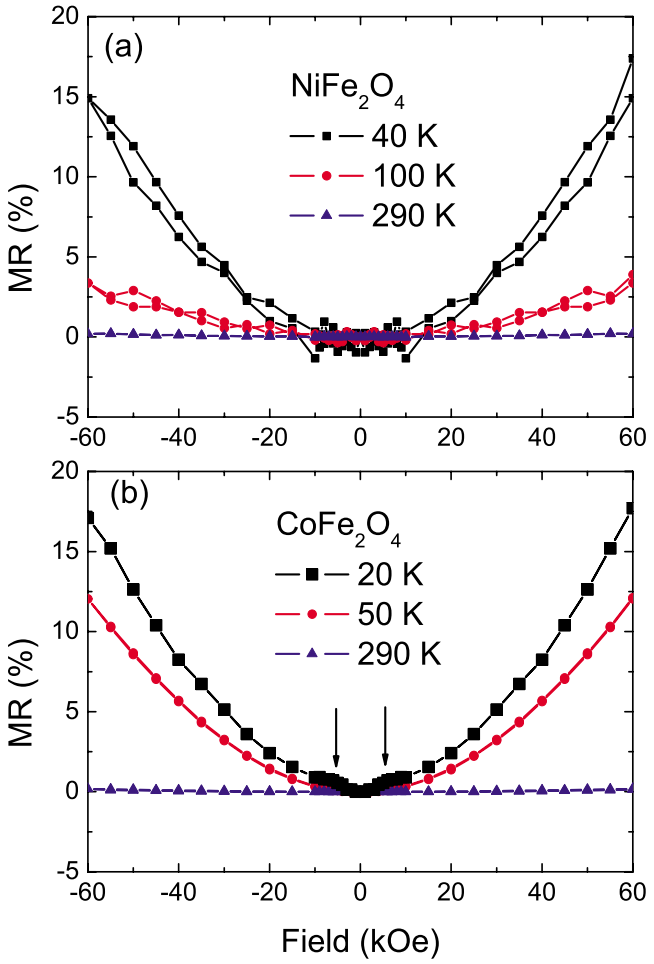

FIG. 13. (Color online) The field dependent MR of (a) the composites of $NiFe_2O_4$ nanocrystals and ZnO and (b) the composites of $CoFe_2O_4$ nanocrystals and ZnO. The solid lines are guides to the eyes.

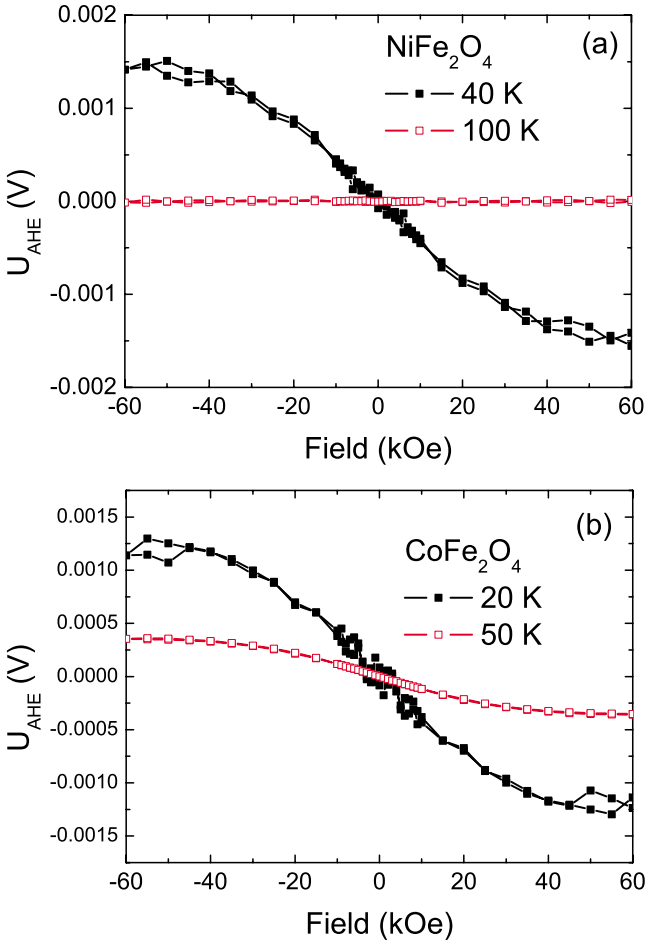

FIG. 14. (Color online) Anomalous Hall voltage vs magnetic field for (a) the composites of $NiFe_2O_4$ nanocrystals and ZnO and (b) the composites of $CoFe_2O_4$ nanocrystals and ZnO.

range from around 77 K to room temperature the $NiFe_2O_4$ single crystals exhibit semiconducting conductivity, and the activation energy is around 60 meV. Figure 12(b) displays the temperature-dependent carrier-concentration and Hall mobility. The sheet electron concentration increases with temperature and reaches to 4.8×10^{13} cm^{-2}. Its temperature dependence can be well fitted by the function e^{-E_a/k_BT}. Figure 12(b) also shows the temperature-dependent mobility. The electron mobility μ reaches a maximum of above 900 cm^2/Vs at 65 K. Actually such large electron mobility and concentration were also observed in ion implanted ZnO (Ref. 56) and in virgin ZnO annealed in N_2.[57]

We also measured the magnetic field dependent resistance (MR) for the composites of $NiFe_2O_4$ ($CoFe_2O_4$) nanocrystal and ZnO as shown in Fig. 13. MR is defined as

$$\mathrm{MR} = (R[H] - R[0])/R[0]. \quad (6)$$

The two samples exhibit a similar MR behavior. Only positive MR has been observed and MR decreases quickly from around 16% (6 T) at 20 or 40 K to 0.2% (6 T) at 290 K. The overall shape of the field-dependent MR is quadratic and shows no sign of saturation. We attribute it to ordinary MR effect resulting from the curving of the electron trajectory due to Lorenz force in a magnetic field. The characteristic quantity is the Landau orbit, $L_H=(eH/\hbar c)^{-1/2}$, which is temperature independent. Another parameter is the dephasing length L_{Th} of electrons, the diffusing distance between two elastic-scattering events, which decreases with increasing temperature. When the dephasing length is much smaller than the Landau orbit, $L_{Th}^2/L_H^2 \ll 1$, the magnetoresistance is quadratic and nonsaturating. Actually the field-dependent MR can be fitted well as a H^2 dependence (not shown). That means the dephasing length is very small in this sample due to the presence of $NiFe_2O_4$ or $CoFe_2O_4$ nanocrystals. In the literature a large positive MR up to several hundreds or thousands percent has been observed in regularly ordered nanowires[58] or nanocolumns.[59] A nonsaturating positive MR effect is expected to be useful for wide-range field sensing. A positive MR has also been observed in Co-doped ZnO films and modelled by considering *s-d* exchange.[55,60] Note that the MR at 20 K in Fig. 13 exhibits a small contribution indicated by the arrows, which saturates at low fields. This contribution could be due to *s-d* exchange considering that a small amount of Co^{2+} or Ni^{2+} ions remains in a diluted state. On the other hand, no negative MR has been observed, which often was found in the hybrid system of MnAs and GaAs.[61,62]

The Hall resistivity

$$\rho_{xy} = R_H B + R_M \mu_0 M \tag{7}$$

is known to be a sum of the ordinary and anomalous Hall terms, where B is magnetic induction, μ_0 is magnetic permeability, M is magnetization, R_H is the ordinary Hall coefficient, and R_M is the anomalous Hall coefficient. The ordinary and anomalous Hall term is linear in B and M, respectively. After subtracting the linear part, the ordinary Hall effect, a clear anomalous Hall effect (AHE) also has been observed in the two samples, as shown in Fig. 14. AHE vanishes at temperatures above 100 K. Obviously the AHE curve does not coincide with the magnetization curve as shown in Figs. 4 and 5. It is difficult to correlate the observed AHE to $NiFe_2O_4$ or $CoFe_2O_4$ nanocrystals. Usually, AHE is not expected or very weak for a semiconductor with embedded magnetic nanoparticles.[63,64] If one considers that the shape of the AHE curves mimics the M-H curves, the AHE is likely due to some paramagnetic contributions or magnetism induced by intrinsic defects.[65]

IV. CONCLUSIONS

(I) Nanoscaled ferrite materials attract considerable research attention due to their cation distribution and applications as dielectric materials.[46,66–68] Usually, ferrite nanoparticles are formed by mechanical or chemical methods. We have demonstrated the formation of $NiFe_2O_4$ and $CoFe_2O_4$ nanocrystals inside a ZnO matrix. Ion-beam synthesis has its own obvious advantage of allowing lateral patterning.[69]

(II) $NiFe_2O_4$ and $CoFe_2O_4$ nanoparticles are crystallographically oriented with respect to the ZnO matrix. They show similar structural properties but different magnetic and transport properties. Considering the rich phases of spinel ferrites ($TMFe_2O_4$, TM=Ni,Co,Fe,Mn,Cu,Zn), our results demonstrate the possibility to have a magnet/semiconductor hybrid system. This system can be tuned over a large variety of magnetic and transport properties. However, the observed MR and AHE are likely not related to the presence of $NiFe_2O_4$ and $CoFe_2O_4$ nanocrystals. This could be due to the imperfect interface between nanocrystals and ZnO matrix. This problem could be solved by epitaxial growth methods, e.g., pulsed laser deposition. A multilayered structure of ferrites/ZnO could be grown and opens a path toward semiconducting spintronic devices.

(III) Our results suggest the possible integration of ferrites with semiconducting ZnO, which would allow the integration of microwave with semiconductor devices. The combination of ferrites and conventional semiconductors, e.g., Si and GaAs, proves to be challenging due to the requirements of oxygen atmosphere and high temperature for ferrites.[11]

Note added. Recently, we observed that an all-oxide ferromagnet/semiconductor (Fe_3O_4/ZnO) heterostructure has been realized by other groups using pulsed laser deposition.[70]

ACKNOWLEDGMENTS

The authors (S.Z., Q.X., and H.S.) gratefully acknowledge financial funding from the Bundesministerium für Bildung und Forschung (FKZ03N8708). Q. X. is supported by the National Natural Science Foundation of China (Grant No. 50802041) and by the National Key Projects for Basic Research of China (Grant No. 2010CB923404). The Advanced Light Source is supported by the Director, Office of Science, Office of Basic Energy Sciences, of the U.S. Department of Energy under Contract No. DE-AC02-05CH11231.

*s.zhou@fzd.de

[1] S. Chikazumi, *Physics of Ferromagnetism* (Oxford University Press, Oxford, 1997).
[2] U. Lüders, A. Barthélémy, M. Bibes, K. Bouzehouane, S. Fusil, E. Jacquet, J. P. Contour, J. F. Bobo, J. Fontcuberta, and A. Fert, Adv. Mater. **18**, 1733 (2006).
[3] S. Zhou, K. Potzger, H. Reuther, G. Talut, F. Eichhorn, J. von Borany, W. Skorupa, M. Helm, and J. Fassbender, J. Phys. D **40**, 964 (2007).
[4] A. L. Geiler, A. Yang, X. Zuo, S. D. Yoon, Y. Chen, V. G. Harris, and C. Vittoria, Phys. Rev. Lett. **101**, 067201 (2008).
[5] M. Ishikawa, H. Tanaka, and T. Kawai, Appl. Phys. Lett. **86**, 222504 (2005).
[6] J. Takaobushi, H. Tanaka, T. Kawai, S. Ueda, J.-J. Kim, M. Kobata, E. Ikenaga, M. Yabashi, K. Kobayashi, Y. Nishino, D. Miwa, K. Tamasaku, and T. Ishikawa, Appl. Phys. Lett. **89**, 242507 (2006).
[7] U. Lüders, M. Bibes, K. Bouzehouane, E. Jacquet, J.-P. Contour, S. Fusil, J.-F. Bobo, J. Fontcuberta, A. Barthélémy, and A. Fert, Appl. Phys. Lett. **88**, 082505 (2006).
[8] A. V. Ramos, M.-J. Guittet, J.-B. Moussy, R. Mattana, C. Deranlot, F. Petroff, and C. Gatel, Appl. Phys. Lett. **91**, 122107 (2007).
[9] E. Snoeck, C. Gatel, R. Serra, G. BenAssayag, J.-B. Moussy, A. M. Bataille, M. Pannetier, and M. Gautier-Soyer, Phys. Rev. B **73**, 104434 (2006).
[10] A. V. Ramos, T. S. Santos, G. X. Miao, M.-J. Guittet, J.-B. Moussy, and J. S. Moodera, Phys. Rev. B **78**, 180402(R) (2008).
[11] Z. Chen, A. Yang, A. Gieler, V. G. Harris, C. Vittoria, P. R. Ohodnicki, K. Y. Goh, M. E. McHenry, Z. Cai, T. L. Goodrich, and K. S. Ziemer, Appl. Phys. Lett. **91**, 182505 (2007).
[12] Y. Suzuki, Annu. Rev. Mater. Res. **31**, 265 (2001).
[13] J. Ziegler, J. Biersack, and U. Littmark, *The Stopping and Range of Ions in Matter* (Pergamon, New York, 1985).
[14] S. Zhou, K. Potzger, J. von Borany, R. Grötzschel, W. Skorupa, M. Helm, and J. Fassbender, Phys. Rev. B **77**, 035209 (2008).
[15] S. Zhou, K. Potzger, G. Talut, H. Reuther, J. von Borany, R. Grötzschel, W. Skorupa, M. Helm, J. Fassbender, N. Volbers, M. Lorenz, and T. Herrmannsdörfer, J. Appl. Phys. **103**, 023902 (2008).
[16] R. Brand, Nucl. Instrum. Methods Phys. Res. B **28**, 398 (1987).
[17] A. Bonanni, A. Navarro-Quezada, T. Li, M. Wegscheider, Z.

Matěj, V. Holý, R. T. Lechner, G. Bauer, M. Rovezzi, F. D'Acapito, M. Kiecana, M. Sawicki, and T. Dietl, Phys. Rev. Lett. **101**, 135502 (2008).
[18] B. D. Cullity, *Elements of X-ray Diffractions* (Addison-Wesley, Reading, 1978).
[19] S. O. Kucheyev, J. S. Williams, C. Jagadish, J. Zou, C. Evans, A. J. Nelson, and A. V. Hamza, Phys. Rev. B **67**, 094115 (2003).
[20] S. Zhou, K. Potzger, D. Buerger, K. Kuepper, M. Helm, J. Fassbender, and H. Schmidt, Nucl. Instrum. Methods, Phys. Res. B **267**, 1620 (2009).
[21] S. Zhou, G. Talut, K. Potzger, A. Shalimov, J. Grenzer, W. Skorupa, M. Helm, J. Fassbender, E. Čižmár, S. A. Zvyagin, and J. Wosnitza, J. Appl. Phys. **103**, 083907 (2008).
[22] Y. J. Li, B. Zhang, W. Lu, Y. Wang, and J. Zou, Appl. Phys. Lett. **93**, 131919 (2008).
[23] Y. Wang, J. Zou, Y. Li, B. Zhang, and W. Lu, Acta Mater. **57**, 2291 (2009).
[24] M. Opel, K.-W. Nielsen, S. Bauer, S. T. Goennenwein, J. C. Cezar, D. Schmeisser, J. Simon, W. Mader, and R. Gross, Eur. Phys. J. B **63**, 437 (2008).
[25] B. Rellinghaus, S. Stappert, E. Wassermann, H. Sauer, and B. Spliethoff, Eur. Phys. J. D **16**, 249 (2001).
[26] E. C. Stoner and E. P. Wohlfarth, IEEE Trans. Magn. **27**, 3475 (1991).
[27] G. A. Candela and R. A. Haines, Appl. Phys. Lett. **34**, 868 (1979).
[28] M. Respaud, J. M. Broto, H. Rakoto, A. R. Fert, L. Thomas, B. Barbara, M. Verelst, E. Snoeck, P. Lecante, A. Mosset, J. Osuna, T. O. Ely, C. Amiens, and B. Chaudret, Phys. Rev. B **57**, 2925 (1998).
[29] W. A. Yager, J. K. Galt, F. R. Merritt, and E. A. Wood, Phys. Rev. **80**, 744 (1950).
[30] R. M. Bozorth, E. F. Tilden, and A. J. Williams, Phys. Rev. **99**, 1788 (1955).
[31] H. T. Jeng and G. Y. Guo, J. Magn. Magn. Mater. **240**, 436 (2002).
[32] Y. Suzuki, R. B. van Dover, E. M. Gyorgy, J. M. Phillips, V. Korenivski, D. J. Werder, C. H. Chen, R. J. Cava, J. J. Krajewski, W. F. Peck, and K. B. Do, Appl. Phys. Lett. **68**, 714 (1996).
[33] J. F. Hochepied, P. Sainctavit, and M. Pileni, J. Magn. Magn. Mater. **231**, 315 (2001).
[34] J. P. Crocombette, M. Pollak, F. Jollet, N. Thromat, and M. Gautier-Soyer, Phys. Rev. B **52**, 3143 (1995).
[35] F. M. F. de Groot, M. Abbate, J. van Elp, G. A. Sawatzky, Y. J. Ma, C. T. Chen, and F. Sette, J. Phys.:Condens. Matter **5**, 2277 (1993).
[36] A. Barla, G. Schmerber, E. Beaurepaire, A. Dinia, H. Bieber, S. Colis, F. Scheurer, J.-P. Kappler, P. Imperia, F. Nolting, F. Wilhelm, A. Rogalev, D. Müller, and J. J. Grob, Phys. Rev. B **76**, 125201 (2007).
[37] G. van der Laan, E. Arenholz, R. V. Chopdekar, and Y. Suzuki, Phys. Rev. B **77**, 064407 (2008).
[38] F. M. F. de Groot, J. Electron Spectrosc. Relat. Phenom. **67**, 529 (1994).
[39] F. M. F. de Groot, Coord. Chem. Rev. **249**, 31 (2005).
[40] G. van der Laan, C. M. B. Henderson, R. A. D. Pattrick, S. S. Dhesi, P. F. Schofield, E. Dudzik, and D. J. Vaughan, Phys. Rev. B **59**, 4314 (1999).
[41] K. Kuepper, I. Balasz, H. Hesse, A. Winiarski, K. C. Prince, M. Matteucci, D. Wett, R. Szargan, E. Burzo, and M. Neumann, Phys. Status Solidi A **201**, 3252 (2004).
[42] A. Gloter, A. Douiri, M. Tence, and C. Colliex, Ultramicroscopy **96**, 385 (2003).
[43] J. Takaobushi, M. Ishikawa, S. Ueda, E. Ikenaga, J.-J. Kim, M. Kobata, Y. Takeda, Y. Saitoh, M. Yabashi, Y. Nishino, D. Miwa, K. Tamasaku, T. Ishikawa, I. Satoh, H. Tanaka, K. Kobayashi, and T. Kawai, Phys. Rev. B **76**, 205108 (2007).
[44] U. Lüders, M. Bibes, J.-F. Bobo, M. Cantoni, R. Bertacco, and J. Fontcuberta, Phys. Rev. B **71**, 134419 (2005).
[45] V. N. Antonov, B. N. Harmon, and A. N. Yaresko, Phys. Rev. B **67**, 024417 (2003).
[46] C. N. Chinnasamy, A. Narayanasamy, N. Ponpandian, K. Chattopadhyay, H. Guerault, and J. M. Greneche, J. Phys.: Condens. Matter **12**, 7795 (2000).
[47] S. J. Kim, S. W. Lee, and C. S. Kim, Jpn. J. Appl. Phys., Part I **40**, 4897 (2001).
[48] N. Ponpandian, A. Narayanasamy, C. N. Chinnasamy, N. Sivakumar, J.-M. Greneche, K. Chattopadhyay, K. Shinoda, B. Jeyadevan, and K. Tohji, Appl. Phys. Lett. **86**, 192510 (2005).
[49] J. P. Chen, C. M. Sorensen, K. J. Klabunde, G. C. Hadjipanayis, E. Devlin, and A. Kostikas, Phys. Rev. B **54**, 9288 (1996).
[50] S. Chakraverty, S. Mitra, K. Mandal, P. M. G. Nambissan, and S. Chattopadhyay, Phys. Rev. B **71**, 024115 (2005).
[51] S. Mitra, K. Mandal, S. Sinha, P. M. G. Nambissan, and S. Kumar, J. Phys. D **39**, 4228 (2006).
[52] A. V. Zalesskii, M. K. Gubkin, T. M. Perekalina, and T. A. Khimich, Crystallogr. Rep. **45**, 678 (2000).
[53] G. H. Kassier, M. Hayes, F. D. Auret, M. Mamor, and K. Bouziane, J. Appl. Phys. **102**, 014903 (2007).
[54] K. Maeda, M. Sato, I. Niikura, and T. Fukuda, Semicond. Sci. Technol. **20**, S49 (2005).
[55] Q. Xu, L. Hartmann, H. Schmidt, H. Hochmuth, M. Lorenz, R. Schmidt-Grund, C. Sturm, D. Spemann, and M. Grundmann, Phys. Rev. B **73**, 205342 (2006).
[56] K. Potzger, K. Kuepper, Q. Xu, S. Zhou, H. Schmidt, M. Helm, and J. Fassbender, J. Appl. Phys. **104**, 023510 (2008).
[57] D. C. Look, B. Claflin, and H. E. Smith, Appl. Phys. Lett. **92**, 122108 (2008).
[58] K. Liu, C. L. Chien, P. C. Searson, and K. Yu-Zhang, Appl. Phys. Lett. **73**, 1436 (1998).
[59] M. Jamet, A. Barski, T. Devillers, V. Poydenot, R. Dujardin, P. Bayle-Guillemaud, J. Rothman, E. Bellet-Amalric, A. Marty, J. Cibert, R. Mattana, and S. Tatarenko, Nature Mater. **5**, 653 (2006).
[60] Q. Xu, L. Hartmann, H. Schmidt, H. Hochmuth, M. Lorenz, D. Spemann, and M. Grundmann, Phys. Rev. B **76**, 134417 (2007).
[61] P. J. Wellmann, J. M. Garcia, J. L. Feng, and P. M. Petroff, Appl. Phys. Lett. **73**, 3291 (1998).
[62] H. Akinaga, J. De Boeck, G. Borghs, S. Miyanishi, A. Asamitsu, W. Van Roy, Y. Tomioka, and L. H. Kuo, Appl. Phys. Lett. **72**, 3368 (1998).
[63] S. R. Shinde, S. B. Ogale, J. S. Higgins, H. Zheng, A. J. Millis, V. N. Kulkarni, R. Ramesh, R. L. Greene, and T. Venkatesan, Phys. Rev. Lett. **92**, 166601 (2004).
[64] S. X. Zhang, W. Yu, S. B. Ogale, S. R. Shinde, D. C. Kundaliya, W.-K. Tse, S. Y. Young, J. S. Higgins, L. G. Salamanca-Riba, M. Herrera, L. F. Fu, N. D. Browning, R. L. Greene, and T. Venkatesan, Phys. Rev. B **76**, 085323 (2007).
[65] Q. Xu, H. Schmidt, S. Zhou, K. Potzger, M. Helm, H. Hochmuth, M. Lorenz, A. Setzer, P. Esquinazi, C. Meinecke, and M.

Grundmann, Appl. Phys. Lett. **92**, 082508 (2008).
[66] S. A. Oliver, H. H. Hamdeh, and J. C. Ho, Phys. Rev. B **60**, 3400 (1999).
[67] M. Bohra, S. Prasad, N. Kumar, D. S. Misra, S. C. Sahoo, N. Venkataramani, and R. Krishnan, Appl. Phys. Lett. **88**, 262506 (2006).
[68] S. Thakur, S. C. Katyal, and M. Singh, Appl. Phys. Lett. **91**, 262501 (2007).
[69] J. Fassbender and J. McCord, J. Magn. Magn. Mater. **320**, 579 (2008).
[70] A. Nielsen, A. Brandlmaier, M. Althammer, W. Kaiser, M. Opel, J. Simon, W. Mader, S. T. B. Goennenwein, and R. Gross, Appl. Phys. Lett. **93**, 162510 (2008).